Journal of Alloys and Compounds 509 (2011) 6768–6772

Contents lists available at ScienceDirect

Journal of Alloys and Compounds

journal homepage: www.elsevier.com/locate/jallcom

Phase range and physical properties of the thallium tin tellurides $Tl_{10-x}Sn_xTe_6$ ($x \leq 2.2$)

Bryan A. Kuropatwa, Abdeljalil Assoud, Holger Kleinke*

Department of Chemistry, University of Waterloo, Waterloo, ON, Canada N2L 3G1

ARTICLE INFO

Article history:
Received 9 March 2011
Received in revised form 24 March 2011
Accepted 24 March 2011
Available online 8 April 2011

Keywords:
Thallium
Tin
Telluride
Semiconductor
Thermoelectric

ABSTRACT

Crystal structures and physical property measurements were determined for $Tl_{10-x}Sn_xTe_6$ with a phase range of $0 \leq x \leq 2.2$. These tellurides are substitution variants of Tl_5Te_3. Electronic structure calculations indicate that $Tl_8Sn_2Te_6$ should be an intrinsic semiconductor, and the Sn-poor variants, extrinsic ones with *p*-type conduction. The positive Seebeck values increase with increasing Sn content, while the electrical and thermal conductivity values decrease. Low thermal conductivity values, well below 1 $W\,m^{-1}\,K^{-1}$, are the best asset of these materials with respect to thermoelectric performance. At $x = 2.2$, the best thermoelectric properties were obtained, with a figure-of-merit $ZT = 0.60$ at 617 K as determined on sintered cold-pressed pellets.

1. Introduction

Thermoelectric materials are capable of transforming a temperature gradient into electricity [1]. As such, the thermoelectric energy conversion may be employed to turn part of the waste heat of automobiles into electricity, thereby enhancing the gas mileage [2,3]. With a narrow band gap semiconducting complex crystal structure, thermoelectric materials are able to pass electrons through the structure while heat, or phonons, become disrupted by the lattice – generally comprised of heavy elements [4]. This enables the materials to convert a heat gradient into electricity or vice versa. The major setback of this energy conversion is the relatively low conversion efficiency, represented by

$$\eta = \frac{T_H - T_C}{T_H} \cdot \frac{\sqrt{1+ZT}-1}{\sqrt{1+ZT}+T_C/T_H},$$

where T_H and T_C represent the respective hot and cold temperatures, T the averaged temperature, and ZT the dimensionless thermoelectric figure-of-merit [1]. ZT can be expressed as the product of three physical properties: Seebeck coefficient, S, electrical conductivity, σ, and total thermal conductivity, κ, according to $ZT = TS^2\sigma/\kappa$. A ZT of 3 would result in an approximate efficiency of 30% assuming a temperature gradient between 300 K and 900 K [5], while the leading current materials currently in use typically max out at $ZT = 1$ [6].

To date, the best thermoelectric materials are made up of heavy anionic *p*-block elements, including antimony [7] and tellurium [8]. Materials of current interest in thermoelectric studies include Zintl phases [9–11], skutterudites including $Ce/LaFe_{4-x}Co_xSb_{12}$ [12], and the LAST ($AgPb_mSbTe_{m+2}$) material [8] with its derivatives [13,14]. Amongst those materials of interest, one will find a number of thallium tellurides including Tl_2GeTe_3 [15], Tl_9AgTe_5 [16], Tl-doped PbTe [17], and $TlSbTe_2$ [18]. Tl_9BiTe_6 [19] and Tl_9LaTe_6 [20], substitution variants of mixed-valent Tl_5Te_3 [21], are narrow band gap semiconductors; strong potential benefits for thermoelectric performance originate from the structure's complex network of heavy atoms [22]. Similarly, studies of the compound Tl_4SnTe_3 [23] ($\equiv Tl_8Sn_2Te_6$) revealed a high thermoelectric figure-of-merit, ZT, culminating in 0.74 at 673 K [24]. This compound was explored with respect to other group 14 elements, Ge and Pb, but not to varying Sn contents. To our knowledge, the system $Tl_{10-x}Sn_xTe_6$ has been studied here for the first time, to investigate the consequences of changing the Tl/Sn ratio.

2. Experimental

2.1. Syntheses

All reactions were prepared from the elements (Tl: 99.99%, granules 1–5 mm, ALDRICH; Sn: 99.8%, powder −325 mesh, ALDRICH; Te: 99.999%, ingot, ALDRICH), with total sample masses between 500 mg and 1000 mg. The $Tl_{10-x}Sn_xTe_6$ system was explored by heating the elements Tl, Sn and Te in their respective stoichiometric molar ratios inside evacuated (approx. 10^{-3} mbar) silica tubes. Fused silica tubes were sealed under a hydrogen–oxygen flame, and samples were heated in resistance furnaces to 650 °C, followed by slow cooling to 470 °C within five days. Those typically mixed-phase samples were crushed into fine powder, resealed in

* Corresponding author.
E-mail address: kleinke@uwaterloo.ca (H. Kleinke).

0925-8388/$ – see front matter © 2011 Elsevier B.V. All rights reserved.
doi:10.1016/j.jallcom.2011.03.182

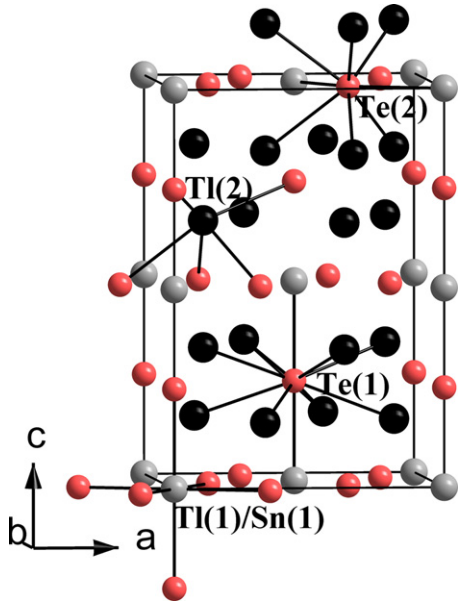

Fig. 1. Unit cell of $Tl_{9.05}Sn_{0.95}Te_6$.

silica tubes and annealed at 450 °C for fifteen days. In order to explore the full phase range of this system, x was increased in increments of 0.2 such that $0 < x < 3.4$.

2.2. Analyses

Phase identifications were carried out by powder X-ray diffractometry (using an INEL diffractometer with position-sensitive detector and Cu $K\alpha_1$ radiation) from well-ground products in all cases. Selected crystals were analyzed by means of standardless energy dispersive spectroscopy (EDXS, LEO 1530, with integrated EDAX Pegasus 1200 detector) using an acceleration voltage of 25 kV, a procedure that verified the existence of the desired elements within the products, and most importantly provided further evidence for increasing Sn content in the $Tl_{10-x}Sn_xTe_6$ series with increasing x until $x = 2.2$. For example, averaged over several crystals, the atomic-% in case of nominal "$Tl_{9.6}Sn_{0.4}Te_6$" were Tl:Sn:Te = 61.1:3.9:35.0 (expected: 60.0:2.5:37.5), for the $x = 1$ case 56.6:6.4:37.0 (expected: 56.3:6.3:37.5), and for the $x = 2.2$ case 53.2:10.5:36.3 (expected: 48.8:13.8:37.5). When $x > 2.2$, the side product SnTe was detected both in the EDXS analyses as well as in the powder diffractogram.

2.3. Crystal structure studies

The data collections were carried out on a BRUKER SMART APEX CCD at room temperature utilizing Mo-Kα radiation. The crystals were picked from two different reactions with different nominal x values (Sn contents), namely from $x = 1$ (crystal 1), and $x = 1.8$ (crystal 2). Data was collected by scans of 0.3° in ω in at least two blocks of 600 frames at $\phi = 0°$ and $\phi = 120°$, with exposure times of 40 s/frame for all three cases. The data was corrected for Lorentz and polarization effects.

Structure refinements were performed with the SHELXTL package [25]. The crystal refinements were completed using the atomic positions published for Tl_9BiTe_6 [19] assuming mixed Tl/Sn occupancies on the 4*c* (M(1)) site and 16*l* (M(2)) site, as was observed for Tl_4SnTe_3 [23]. Attempts to include Sn on the 16*l* site of crystal 1 resulted in a negative occupancy factor for Sn within its standard deviation, so that the occupancy was assumed to be 100% Tl. Refinements converged smoothly without showing any abnormalities. In the case of nominal Tl_9SnTe_6 (crystal 1), the refined x value of 0.95(8) equals the nominal one within one standard deviation. For crystal 2, the refined $x = 1.63(9)$ is within two standard deviations of the nominal $x = 1.8$.

As no suitable single crystals were obtained, we performed Rietveld refinements [26] using the GSAS program [27,28] via the graphical interface EXPGUI [29] of the samples with nominal $x = 2.0$ and $x = 2.2$. Data were collected on the above-mentioned INEL diffractometer for 16 h in each case. The refined formulas are $Tl_{8.0}Sn_{2.0(3)}Te_6$ and $Tl_{7.5}Sn_{2.5(3)}Te_6$, respectively. Crystallographic details are summarized in Table 1, the atomic positions, isotropic displacement parameters and Sn occupancies of $Tl_{10-x}Sn_xTe_6$ in Table 2. Further details of the crystal structure investigations can be obtained from the Fachinformationszentrum Karlsruhe, 76344 Eggenstein-Leopoldshafen, Germany (fax: +49 7247 808 666; e-mail: crysdata@fiz-karlsruhe.de) on quoting the depository numbers CSD-422128 (nominal $x = 1.0$) and 422129 (nominal $x = 1.8$).

2.4. Electronic structure calculations

Self-consistent tight-binding *first principles* LMTO calculations (LMTO = linear muffin tin orbitals) were performed using the atomic spheres approximation (ASA) [30,31] to study the impact of Sn addition on the band gaps. In the LMTO approach, the density functional theory is used with the local density approximation (LDA) for the exchange correlation energy [32]. Three different models were calculated. The initial binary compound, $Tl_{10}Te_6$ (*I*4/*mcm*), was first calculated and then compared to the two ternary tellurides Tl_9SnTe_6 (*I*4/*m*) and $Tl_8Sn_2Te_6$ (*I*4/*mcm*). The wavefunctions used in the calculations are as follows: for Tl 6*s*, 6*p*, 6*d* and 5*f*; for Sn 5*s*, 5*p*, and 5*d* and 4*f*, and for Te 5*s*, 5*p*, and 5*d* and 4*f*. The eigenvalue problems were solved on the basis of 512*k* points within the irreproducible wedge of the first Brillouin zone, respectively, selected with an improved tetrahedron method [33].

2.5. Physical property measurements

2.5.1. Seebeck measurement on Tl_5Te_3

A cold-pressed bar with dimensions of 6 mm × 1 mm × 1 mm was utilized after applying silver paint (Ted Pella) to create the electric contacts. A commercial thermopower measurement apparatus (MMR Technologies) was used, measuring the Seebeck coefficient (S) under dynamic vacuum in the temperature range of 300–550 K with constantan as an internal standard, to determine the temperature difference.

2.5.2. Seebeck and electrical conductivity measurements

Part of the ground phase-pure samples were cold-pressed into bar-shaped pellets of the dimensions 13 × 2 × 2 [in mm] for Seebeck coefficient (S) and electrical conductivity (σ) measurements, simultaneously determined utilizing the ULVAC-RIKO ZEM-3 under helium between room temperature and 550 K. Estimated errors are ±2 μV K^{-1} for S and ±3% the electrical conductivity. Cold-pressed pellet densi-

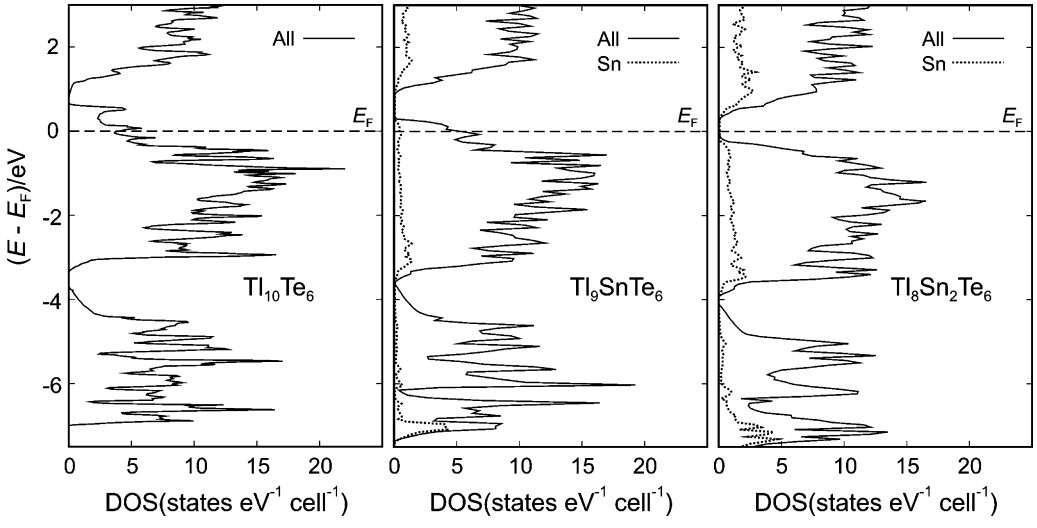

Fig. 2. Densities of states (DOS) of $Tl_{10}Te_6$ (left), Tl_9SnTe_6 (center) and $Tl_8Sn_2Te_6$ (right). The dashed horizontal lines indicate the Fermi energy, E_F.

Table 1
Crystallographic data for $Tl_{10-x}Sn_xTe_6$.

Chemical formula	$Tl_{9.05}Sn_{0.95(8)}Te_6$	$Tl_{8.37}Sn_{1.63(9)}Te_6$	$Tl_{8.0}Sn_{2.0(3)}Te_6$	$Tl_{7.5}Sn_{2.5(3)}Te_6$
Formula weight [g/mol]	2727.90	2669.64	2639.4	2599.08
T of measurement [K]	296(2)	296(2)	296(2)	296(2)
λ [Å]	0.71073	0.71073	1.5406	1.5406
Space group	*I*4/*mcm*	*I*4/*mcm*	*I*4/*mcm*	*I*4/*mcm*
a [Å] = b	8.8416(6)	8.850(1)	8.8384(4)	8.8375(1)
c [Å]	13.0114(9)	13.059(2)	13.0525(6)	13.0585(3)
V [Å^3]	1017.2(1)	1022.9(2)	1019.6(1)	1019.88(2)
Z	2	2	2	2
$R(F_o)^a/R_w(F_o^2)^b$	0.064/0.154	0.024/0.057		
$R_P{}^c/R_B{}^d$			0.052/0.097	0.060/0.112

[a] $R(F_o) = \sum ||F_o| - |F_c|| / \sum |F_o|$, [b] $R_w(F_o^2) = [\sum [w(F_o^2 - F_c^2)^2] / \sum [w(F_o^2)^2]]^{1/2}$, [c] $R_P = \sum |y_o - y_c| / \sum |y_o|$, [d] $R_B = \sum |I_o - I_c| / \sum |I_o|$, with F = structure factor, w = weighing factor, y = intensity (per step/channel), I = intensity (per reflection).

Table 2
Atomic positions, isotropic displacement parameters and Sn occupancies for $Tl_{10-x}Sn_xTe_6$.

Formula	Atom	Site	% Sn on site	x	y	z	U_{eq}/Å^2
$Tl_{9.05}Sn_{0.95}Te_6$	M(1)	4*c*	48.0(4)	0	0	0	0.026(1)
	M(2)	16*l*	0	0.1465(1)	0.6465(1)	0.1593(1)	0.035(1)
	Te(1)	4*a*	–	0	0	0.2500	0.028(1)
	Te(2)	8*h*	–	0.3369(3)	0.8369(3)	0	0.027(1)
$Tl_{8.37}Sn_{1.63}Te_6$	M(1)	4*c*	70.6(10)	0	0	0	0.028(3)
	M(2)	16*l*	2.8(9)	0.1463(3)	0.6463(3)	0.1585(3)	0.034(2)
	Te(1)	4*a*	–	0	0	0.2500	0.024(3)
	Te(2)	8*h*	–	0.3368(6)	0.8368(6)	0	0.024(3)
$Tl_{8.0}Sn_{2.0}Te_6$	M(1)	4*c*	72(4)	0	0	0	0.011(4)
	M(2)	16*l*	7(3)	0.1471(2)	0.6471(2)	0.1605(3)	0.021(1)
	Te(1)	4*a*	–	0	0	0.2500	0.010(3)
	Te(2)	8*h*	–	0.3361(4)	0.8361(4)	0	0.013(3)
$Tl_{7.5}Sn_{2.5}Te_6$	M(1)	4*c*	84(4)	0	0	0	0.014(5)
	M(2)	16*l*	10(3)	0.1469(2)	0.6469(2)	0.1609(4)	0.026(2)
	Te(1)	4*a*	–	0	0	0.2500	0.024(4)
	Te(2)	8*h*	–	0.3376(5)	0.8376(5)	0	0.025(5)

ties ranged between 80 and 85% of the theoretical (calculated) densities of Tl_9SnTe_6 or $Tl_8Sn_2Te_6$ structures depending on the quantity of x. The pellets were annealed at 653 K over a period of 24 h in evacuated fused silica tubes. The densities slightly increased upon sintering of these pellets.

2.5.3. Thermal conductivity measurements

Sample powders were cold pressed into disks comprised of a 6 mm diameter and a 1 mm depth, and then sintered at 653 K like the bars for the ZEM measurements. Thermal diffusivity, D, was measured with the Anter FL3000 under a flow of argon, with an estimated error of ±3%. The thermal conductivity, κ, was calculated via $\kappa = C_p D \rho$, with ρ being the density and C_p the specific heat, obtained from the Dulong-Petit approximation. Sample densities were calculated via the mass of the cold-pressed pellet divided by the pellet volume.

3. Results and discussion

3.1. Crystal structures

The crystal structure of $Tl_{9.05}Sn_{0.95}Te_6$ is shown in Fig. 1, with a 1:1 ratio of Tl:Sn located on the 4*c* Wyckoff site, while the second Tl site (M(2), 16*l*) contains no Sn. There are no Te–Te bonds in this system. The Tl(1)/Sn(1) atoms are coordinated to four Te(1) (3.25 Å) and two Te(2) atoms (3.31 Å) via an octahedral coordination elongated along the *c* direction (Table 3). The M(2) atoms are surrounded by five Te atoms with bond lengths between 3.16 Å and 3.58 Å. The structures contain weak Tl–Tl bonds between 3.5 Å and 3.7 Å forming 2 Tl_8 clusters per unit cell, analogous to elemental S_8 crowns. Tl–Tl bonds are formed only with M(2), not with M(1), which contains a higher quantity of Sn in all cases.

3.2. Electronic structures

In the cases of Tl_5Te_3 and $Tl_8Sn_2Te_6$, the space group was set to *I*4/*mcm* corresponding to the most accurate crystallographic data [34]. Tl_9SnTe_6 was calculated in *I*4/*m*. Due to the lack of Te–Te bonds in the system, the Te atoms are formally fully reduced and all anion charges are then balanced by cation charges in the $x = 2$ case via $(Tl^+)_8(Sn^{2+})_2(Te^{2-})_6$.

Table 3
Bond distances [Å] for $Tl_{10-x}Sn_xTe_6$.

Bond	$Tl_{9.05}Sn_{0.95}Te_6$	$Tl_{8.37}Sn_{1.63}Te_6$	$Tl_{8.0}Sn_{2.0}Te_6$	$Tl_{8.5}Sn_{2.5}Te_6$
M(1)–Te(1) × 2	3.2529(2)	3.2647(4)	3.2631(2)	3.26464(7)
M(1)–Te(2) × 4	3.310(1)	3.3122(5)	3.305(2)	3.311(2)
M(2)–Te(2)	3.156(3)	3.1576(7)	3.157(4)	3.177(5)
M(2)–Te(2) × 2	3.436(3)	3.4370(6)	3.459(4)	3.450(5)
M(2)–Te(1) × 2	3.583(1)	3.592(1)	3.576(2)	3.575(2)
M(2)–M(2)	3.506(3)	3.5278(9)	3.475(6)	3.473(8)
M(2)–M(2) × 2	3.503(4)	3.5230(7)	3.496(6)	3.487(7)
M(2)–M(2)	3.664(4)	3.6621(9)	3.677(4)	3.671(5)

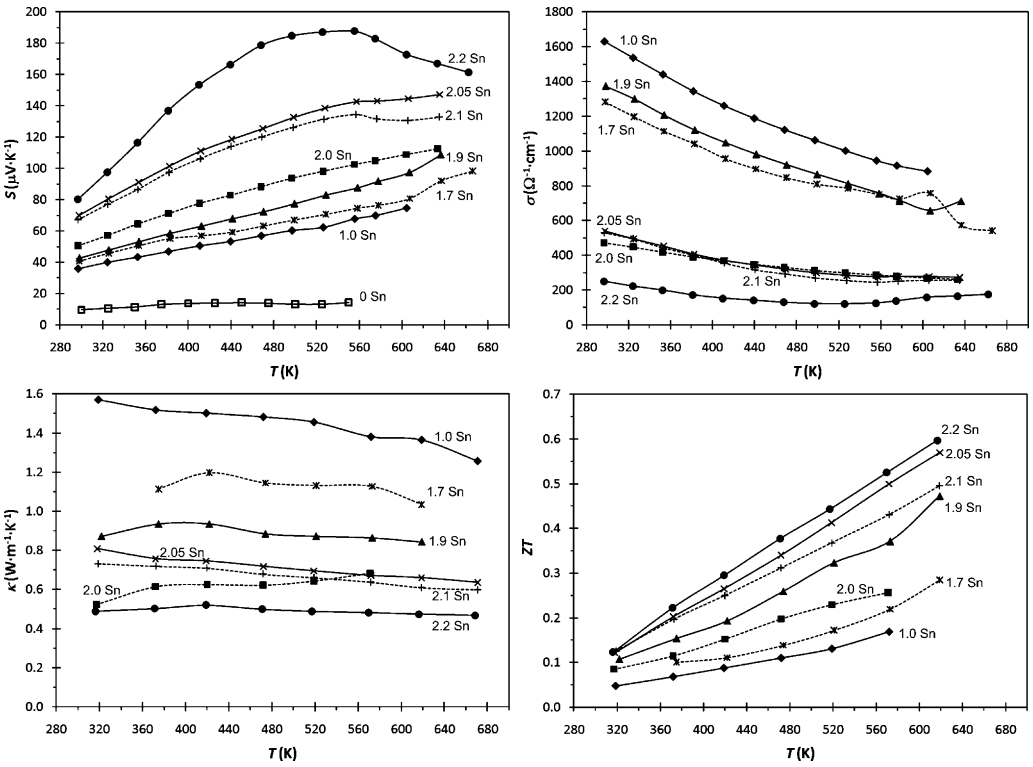

Fig. 3. Thermoelectric properties of $Tl_{10-x}Sn_xTe_6$: Seebeck coefficient (upper left), electrical conductivity (upper right), thermal conductivity (lower left), dimensionless figure of merit (lower right).

The density of states (DOS) calculated for the $Tl_{10}Te_6$ model predicts metallic properties with the Fermi level approximately 0.7 eV significantly below the band gap (Fig. 2). The partially empty valence band is predominantly occupied by Te-*p* states. As the Sn content is increased to 1 (Tl_9SnTe_6), the structure remains metallic with the Fermi level now approximately 0.3 eV below the band gap. The $Tl_8Sn_2Te_6$ model has its Fermi level directly at the band gap, in accord with the results of an earlier Extended Hückel calculation [35].

3.3. Physical properties

The positive Seebeck coefficient, *S*, increases smoothly with increasing temperature for the $Tl_{10-x}Sn_xTe_6$ samples with $x < 2.1$, typical for *p*-type semiconductors having high charge carrier concentration (top left of Fig. 3). The Seebeck curve of the sample with $x = 2.2$ exhibits a clear maximum of $S = +190\ \mu V\,K^{-1}$ around 555 K. Increasing the Sn content, *x*, leads to an increase in *S*, e.g. around room temperature from $S = +10\ \mu V\,K^{-1}$ for $x = 0$ to $S = +80\ \mu V\,K^{-1}$ for $x = 2.2$. The only exception is the sample with $x = 2.05$, whose *S* values are slightly larger than those of the $x = 2.1$ case, e.g. around room temperature 70 $\mu V\,K^{-1}$ vs. 67 $\mu V\,K^{-1}$. This small difference is within experimental error.

The different temperature behavior as *x* is varied can be attributed to the relationship between Seebeck coefficient and temperature and charge carrier concentration displayed below [36]:

$$S = \frac{8\pi^2 k_B^2}{3eh^2} m^* \cdot T\left(\frac{\pi}{3n}\right)^{2/3}.$$

Here, k_B = Boltzmann constant, *e* = electron charge, *h* = Planck constant, m^* = effective mass, *n* = charge carrier concentration. Hence the samples with high, and thus temperature independent *n* (small *x*), will exhibit a linearly increasing Seebeck coefficient with temperature; those with small *n* (large *x*) that increases with temperature, show a decrease in *S*, once sufficient charge carriers are able to cross the gap. Using $E_{gap} = 2eS_{max}T_{max}$ [37], a gap of 0.2 eV results for $Tl_{7.8}Sn_{2.2}Te_6$. Following the aforementioned logic, $x = 2.2$ would yield $(Tl^+)_{7.8}(Sn^{2+})_{2.2}(Te^{2-})_6(e^-)_{0.2}$ leaving an overall electron excess of 0.2 in the proposed formula and hence *n*-type conduction, in contrast to the experimentally observed *p*-type conduction. It is noted that we also observed *p*-type carriers in the isostructural $Tl_{8.85}La_{1.15}Te_6$ that also formally contained excess electrons [20]. Some side products may be present below the detection limit of diffraction studies; for attempted $x > 2.2$, this entails one additional phase – SnTe, which is present between 3 and 6% for "$Tl_{7.6}Sn_{2.4}Te_6$" as found in its diffraction pattern. Moreover, there may be some vacancies in the structure that change the details of the band structure and the charge carrier concentration that may cause the experimentally observed *p*-type conduction.

The 300 K *S* value of +50 $\mu V\,K^{-1}$ obtained from the sintered pellet of $Tl_8Sn_2Te_6$ is significantly below the 80 $\mu V\,K^{-1}$ obtained from (low temperature measurements on) a polycrystalline ingot [38] and the 126 $\mu V\,K^{-1}$ obtained at 323 K from a hot-pressed pellet of 91% density [24]. The Seebeck coefficient of the latter continues to increase until 673 K (the end of the measurement), exceeding +200 $\mu V\,K^{-1}$. The differences at room temperature may be due to slight variations in the exact Tl/Sn ratio and hence the charge carrier concentration, implying that the sample investigated here had higher charge carrier concentration while nominally the same formula. Interestingly, the polycrystalline ingot with an experimentally determined carrier concentration of $2.22 \times 10^{19}\ cm^{-3}$ has the same room temperature Seebeck coefficient as $Tl_{7.8}Sn_{2.2}Te_6$.

The electrical conductivity, σ, for the $Tl_{10-x}Sn_xTe_6$ samples with $x < 2.1$ decreases with increasing temperature (top right of Fig. 3), again evidence of a relatively high carrier concentration. $Tl_{7.8}Sn_{2.2}Te_6$ is again the exception, its σ value reaching a minimum of 121 $\Omega^{-1}\,cm^{-1}$ at 526 K. Thereafter, its increasing number of intrinsic, thermally activated carriers reverses the trend, causing increasing electrical conductivity. This change was not observed

by Kosuga et al. in case of the hot-pressed pellet of $Tl_8Sn_2Te_6$ [24]. Increasing x causes a decrease in σ, in accord with our expectations and the opposite trend in S. Tl_9SnTe_6 displays the highest value ($1630\ \Omega^{-1}\ cm^{-1}$) at room temperature, and $Tl_{7.8}Sn_{2.2}Te_6$ the lowest with $250\ \Omega^{-1}\ cm^{-1}$, and the samples with $x = 2.05$ and 2.1 have almost identical values of $540\ \Omega^{-1}\ cm^{-1}$ and $532\ \Omega^{-1}\ cm^{-1}$, respectively. For comparison, the corresponding values for the $Tl_8Sn_2Te_6$ ingot and hot-pressed pellet are $275\ \Omega^{-1}\ cm^{-1}$ and $272\ \Omega^{-1}\ cm^{-1}$ (at 323 K), respectively.

The thermal conductivity curves (bottom left of Fig. 3) roughly follow the same trend as the electrical conductivity, with Tl_9SnTe_6 displaying the highest and $Tl_{7.8}Sn_{2.2}Te_6$ the lowest values. The values around 317 K range from $1.57\ W\ m^{-1}\ K^{-1}$ to $0.49\ W\ m^{-1}\ K^{-1}$,, which decrease slightly for the most part with increasing temperature. The thermal conductivity of the hot-pressed pellet was determined to be basically temperature independent around $0.5\ W\ m^{-1}\ K^{-1}$ [24], while the one of the polycrystalline ingot was not measured.

The thermoelectric (dimensionless) figure-of-merit, ZT, was calculated from the above-mentioned S, σ, and κ data, by computing polynomial fits for $S^2\sigma$, because κ was measured at different temperatures. In order to avoid extrapolation, only the data points that were both within the temperature range of $S^2\sigma$ and κ were considered. Overall, the ZT trends display a gradual increase with increasing temperature (bottom right of Fig. 3). Tl_9SnTe_6 exhibits the lowest figure-of-merit $ZT = 0.05$ at 319 K, increasing smoothly to 0.17 at 572 K. For the most part, ZT gradually increases with increasing x such that $Tl_{7.8}Sn_{2.2}Te_6$ attains 0.12 at 316 K and 0.60 at 617 K. Hot-pressed $Tl_8Sn_2Te_6$ exhibited $ZT = 0.28$ at 323 K, which increased to 0.67 at 623 K and culminated in 0.74 at 673 K [24].

4. Conclusion

Various members of the $Tl_{10-x}Sn_xTe_6$ series were successfully synthesized, analyzed and their physical properties measured for $x = 1.0$, 1.7, 1.9, 2.0, 2.05, 2.1 and 2.2. The materials are isostructural with the binary telluride Tl_5Te_3, and the crystal structure of Tl_9SnTe_6 was determined with the experimental formula $Tl_{9.05}Sn_{0.95}Te_6$, possessing the same space group ($I4/mcm$) as Tl_5Te_3 and $Tl_8Sn_2Te_6$, in contrast to Tl_9SbTe_6 that adopts the space group $I4/m$.

The band structure calculations for Tl_9SnTe_6 and $Tl_8Sn_2Te_6$ suggest that Tl_9SnTe_6 is a heavily doped p-type semiconductor with a partially empty valence band, while the Fermi level in $Tl_8Sn_2Te_6$ is located in the band gap. In accord with these calculations, both thermal and electrical conductivity measurements indicate that increasing Sn results in lower values, as determined on sintered polycrystalline samples. The opposite trend is visible with respect to the Seebeck coefficient, as increasing x will result in higher values.

The figure-of-merit reaches a maximum at the Sn-rich end of the phase width: $Tl_{7.8}Sn_{2.2}Te_6$ reaches its maximum $ZT = 0.60$ at 617 K (end of measurement), significantly larger than ZT of $Tl_8Sn_2Te_6$ prepared and treated analogously, which remains under 50% of the ZT values of $Tl_{7.8}Sn_{2.2}Te_6$ at elevated temperatures. The fact, that hot-pressed $Tl_8Sn_2Te_6$ was reported to reach 0.67 at 623 K [24], implies that hot-pressing of $Tl_{7.8}Sn_{2.2}Te_6$ should ultimately result in higher values.

Acknowledgments

Financial support from NSERC and General Motors of Canada, is appreciated. We are particularly grateful for the insightful discussions with Dr. J.R. Salvador, Dr. J. Yang and Dr. G.P. Meisner from the General Motors R&D Center, Warren, MI.

Appendix A. Supplementary data

Supplementary data associated with this article can be found, in the online version, at doi:10.1016/j.jallcom.2011.03.182.

References

[1] D.M. Rowe, Thermoelectrics Handbook: Macro to Nano, CRC Press, Taylor & Francis Group, Boca Raton, FL, USA, 2006.
[2] L.E. Bell, Science 321 (2008) 1457–1461.
[3] J. Yang, T. Caillat, Mater. Res. Bull. 31 (2006) 224–229.
[4] T.M. Tritt, in: D.M. Rowe (Ed.), CRC Handbook on Thermoelectrics, CRC Press, Boca Raton, FL, USA, 2005.
[5] F.J. DiSalvo, Science 285 (1999) 703–706.
[6] F. Gascoin, J. Rasmussen, G.J. Snyder, J. Alloys Compd. 427 (2007) 324–329.
[7] H. Kleinke, Chem. Mater. 22 (2010) 604–611.
[8] E. Quarez, K.-F. Hsu, R. Pcionek, N. Frangis, E.K. Polychroniadis, M.G. Kanatzidis, J. Am. Chem. Soc. 127 (2005) 9177–9190.
[9] S.M. Kauzlarich, S.R. Brown, G.J. Snyder, Dalton Trans. (2007) 2099–2107.
[10] E.S. Toberer, A.F. May, G.J. Snyder, Chem. Mater. 22 (2010) 624–634.
[11] H. Xu, K.M. Kleinke, T. Holgate, H. Zhang, Z. Su, T.M. Tritt, H. Kleinke, J. Appl. Phys. 105 (2009), 053703/053701–053703/053705.
[12] B.C. Sales, D. Mandrus, R.K. Williams, Science 272 (1996) 1325–1328.
[13] P.F.P. Poudeu, J. D'Angelo, A.D. Downey, J.L. Short, T.P. Hogan, M.G. Kanatzidis, Angew. Chem. Int. Ed. 45 (2006) 3835–3839.
[14] M.G. Kanatzidis, Chem. Mater. 22 (2010) 648–659.
[15] K.O. Klepp, P. Ecker, J. Solid State Chem. 117 (1995) 351–355.
[16] K. Kurosaki, A. Kosuga, H. Muta, M. Uno, S. Yamanaka, Appl. Phys. Lett. 87 (2005), 061919/061911–061919/061913.
[17] J.P. Heremans, V. Jovovic, E.S. Toberer, A. Saramat, K. Kurosaki, A. Charoenphakdee, S. Yamanaka, G.J. Snyder, Science 321 (2008) 554–557.
[18] K. Kurosaki, H. Uneda, H. Muta, S. Yamanaka, J. Alloys Compd. 376 (2004) 43–48.
[19] T. Doert, P. Böttcher, Z. Kristallogr. 209 (1994) 95.
[20] S. Bangarigadu-Sanasy, C.R. Sankar, A. Assoud, H. Kleinke, Dalton Trans. 40 (2011) 862–867.
[21] I. Schewe, P. Böttcher, H.G. von Schnering, Z. Kristallogr. 188 (1989) 287–298.
[22] B. Wölfing, C. Kloc, J. Teubner, E. Bucher, Phys. Rev. Lett. 86 (2001) 4350–4353.
[23] S. Bradtmöller, P. Böttcher, Z. Anorg, Allg. Chem. 619 (1993) 1155–1160.
[24] A. Kosuga, K. Kurosaki, H. Muta, S. Yamanaka, J. Appl. Phys. 99 (2006), 063705/063701–063705/063704.
[25] G.M. Sheldrick, SHELXTL, Version 5.12 ed., Siemens Analytical X-Ray Systems, Madison, WI, 1995.
[26] R.B. von Dreele, J.D. Jorgensen, C.G. Windsor, J. Appl. Crystallogr. 15 (1982) 581–589.
[27] L.C. Larson, R.B. von Dreele, LANSCE, MSH805, Los Alamos National Laboratory, NM 87545, USA, 1995.
[28] A.C. Larson, R.B. von Dreele, Los Alamos National Laboratory, Los Alamos, NM, 2000.
[29] B.H. Toby, J. Appl. Crystallogr. 34 (2001) 210–213.
[30] O.K. Andersen, Phys. Rev. B 12 (1975) 3060–3083.
[31] H.L. Skriver, The LMTO Method, Springer, Berlin, Germany, 1984.
[32] L. Hedin, B.I. Lundqvist, J. Phys. C 4 (1971) 2064–2083.
[33] P.E. Blöchl, O. Jepsen, O.K. Andersen, Phys. Rev. B 49 (1994) 16223–16233.
[34] S. Bhan, K. Schubert, J. Less-Common Met. 20 (1970) 229–235.
[35] K.J. Nordell, G.J. Miller, J. Alloys Compd. 241 (1996) 51–62.
[36] G.J. Snyder, E.S. Toberer, Nat. Mater. 7 (2008) 105–114.
[37] H.J. Goldsmid, J.W. Sharp, J. Electron. Mater. 28 (1999) 869–872.
[38] M.S.E. Dichi, G. Kra, J. Alloys Compd. 458 (2008) 109–114.